Sonochemical decontamination of magnesium and magnesium-zirconium alloys in mild conditions

Ran Ji, Matthieu Virot, Rachel Pflieger, Sergey I. Nikitenko

Sonochemical Decontamination of Magnesium and Magnesium-Zirconium Alloys in Mild Conditions

Ran Ji, Matthieu Virot,* Rachel Pflieger, Sergey I Nikitenko

ICSM, Univ Montpellier, UMR 5257, CEA, CNRS, ENSCM, Marcoule, France
*matthieu.virot@cea.fr

Abstract

UNGG cladding nuclear wastes constitute a huge volume of Mg-based materials that raises economic and safety concerns, particularly due to their radioactivity coupled to the potential generation of H_2 gas under deep underground disposal. Their significant decontamination would result in more secure and less expensive storage, with a better containment of the separated long-lived radioisotopes that could enter in a classical channel. Sonication of genuine UNGG cladding materials and simulants at 345 kHz in 0.01 M oxalic acid solution (20 °C) allowed the structuring of their surfaces with the observation of homogeneously distributed craters of 20-40 µm in diameter. After a thorough characterization and comparison of the ultrasound effects generated at the surface, the various samples were artificially contaminated and characterized before sonication. The complete and rapid sonochemical decontamination of Mg-based materials was then observed, in addition to the removal of the carbon layer promoting corrosion on the inner UNGG cladding. The extension of sonication allows the neo-formed brucite ($Mg(OH)_2$) and zirconium-based phases to accumulate on the surface, thus contributing in a slight but continuous surface recontamination process. This phenomenon results from the re-adsorption of uranyl cations from the solution which can be avoided by optimizing the duration of treatment.

1. Introduction

Natural Uranium Graphite Gas (UNGG) reactors constitute the first generation of nuclear power plants operated in France for civilian and military purposes after the Second World War (Breeze, 2017; Rastoin and Brisbois, 1978). These reactors used natural graphite as moderator, air or CO_2 as coolant and metallic natural uranium as nuclear fuel, which was packed in a cylinder form in a Mg-Zr (0.5 wt.% Zr) alloy cladding tube sealed with Mg-Mn (1.2 wt.% Mn) plug ends (contrary to the Magnox design, which used Mg/Al alloy in Great Britain) (Chartier et al., 2017; Lambertin et al., 2012; Rastoin and Brisbois, 1978). Second generation of Mg claddings were additionally covered on the inner side by a graphite-based coating named “aquadag” which was directly in contact with U fuel to prevent radionuclides diffusion into the Mg matrix. The operation and dismantling of the nine implemented reactors that used this technology between 1956 and 1994 in France produced a large amount of radioactive nuclear wastes (e.g., metal structural wastes, spent fuel, graphite bricks, radioactive gases…) (Cannes et al., 2019; Chartier et al., 2017; Moncoffre et al., 2016; Muzeau et al.; Pageot et al., 2015; Rooses et al., 2013). Particularly, contaminated Mg-based claddings constitute significant volumes of wastes that have been temporarily stored in the French nuclear sites of Marcoule and La Hague, prior to their conditioning and long-term storage (Chartier et al., 2017; Lambertin et al., 2012; Lambertin et al., 2016; Muzeau et al.).

One of the treatment options currently being considered is the encapsulation of Mg materials in Portland cement or in an aluminosilicate geopolymer prior to deep underground storage (Cannes et al., 2019; Chartier et al., 2017; Lambertin et al., 2012; Lambertin et al., 2016). However, such an approach is cost-intensive and does not guarantee the absence of long-term corrosion between Mg and residual traces of water (Chartier et al., 2017; Lambertin et al., 2012; Song and Atrens, 2003). Mg exhibits a poor corrosion resistance and is indeed a highly reactive metal that can produce hydrogen gas when combined with water (reaction **Eq. 1**) resulting in container deformation, radioactive leakages and explosions in the most extreme cases (Chartier et al., 2017; Hallam et al., 2016; Lambertin et al., 2012; Rooses et al., 2013). Moreover, the consequent release of radioactive particles would lead to dramatic environmental issues. The integrity of the encapsulating matrix or the container may further be modified in the presence of carbon (explosion as reported by D'Amico et al. (2016) or galvanic corrosion as reported by Lambertin et al. (2016) or Chartier et al. (2017)) and the influence of highly radioactive radionuclides that have attached or migrated into the Mg cladding materials. In order to improve the safety and possibly reduce the financial cost of such storage, one alternative consists in the significant decontamination of Mg materials prior to their conditioning. Such a decrease in the level of radioactivity of nuclear waste could imply a new technological strategy with a final ground storage that would be safer and much less expensive. In parallel, one can imagine that a sufficient decrease of the activity level would allow the reuse of such materials in both nuclear and civilian domains (Morris, 2011).

$$Mg + 2\ H_2O \rightarrow Mg(OH)_2 + H_2 \qquad (\Delta G° = -359\ kJ/mol) \quad \textbf{(1)}$$

Surface cleaning is probably the most famous application of ultrasound since its first industrial uses in the 50s (Bulat, 1974; Fuchs, 2015; Mason, 2016; Yao et al., 2020). Ultrasound-assisted removal of surface contaminants is now widely used in many fields, including electronics for printed circuits, optics for precision instruments, jewelry washing, industrial machinery and metal washing, etc. Compared to other techniques (spray, immersion, agitation, etc.), ultrasonic cleaning is advantageous because it is adapted to complex surface shapes, offers access to small cavities and hidden areas, avoids the use of concentrated and hazardous solvents and proposes milder conditions for the treated materials and the operator (Fuchs, 2000; Fuchs, 2015; Mason, 2016; Yao et al., 2020). Despite the democratization of ultrasonic cleaning applications and devices, the characterization, understanding and capabilities of the generated processes at the solid/liquid interface are still unclear. More particularly, reports on ultrasound-assisted decontamination in nuclear industry are very rare in the literature and most of the few applications described often deal with local optimization rather than scientific rationalization. Nevertheless, a very interesting inventory of successful applications in Russian nuclear engineering has been described by Lebedev et al. (2017) and demonstrates the advantages of ultrasound for cleaning, decontamination, reduction of friction during manufacturing, facilitating manipulation, etc. The successful treatment of uranium films deposited by electrolysis on inox samples has also been reported by Van Nguyen et al. (2019). Finally, the successful treatment of low-level radioactive wastewater by standing ultrasonic waves demonstrated a decontamination efficiency of 97.7% from radioactive fine particles with a decrease of activity from 400 to 9.3 $Bq.L^{-1}$ (Su-xia et al., 2014).

Most ultrasonic cleaning approaches are performed in the 20-200 kHz frequency range which is directly related to the phenomenon of acoustic cavitation (i.e., the nucleation, growth and rapid implosive collapse of gas and vapor filled microbubbles) (Fuchs, 2015; Mason, 2016; Mason et al., 2011). The size of the particles that can be removed from a surface generally decreases with increasing ultrasonic frequency, moving from industrial cleaning applications (machined parts, equipment...) to more critical ones (medical, disk drives...) (Fuchs, 2015; Mason et al., 2011). Above ca. 345 kHz, the effects of the ultrasonic cleaning reach Megasonic technology where the cleaning mechanism minimizes cavitation effect (without generation of damages) by means of acoustic streamings (favored for Si wafers, precision optical…) as reported by Brems et al. (2014) and Fuchs (2015). Nevertheless, several studies demonstrated that both physical and chemical effects driven by the implosive collapse of acoustic bubbles could significantly affect material surfaces in the 20-1000 kHz range (Ji et al., 2018; Mazue et al., 2011; Moutarlier et al., 2020; Moutarlier et al., 2015; Virot et al., 2010; Virot et al., 2011; Virot et al., 2012). The operating ultrasonic conditions, and particularly the applied acoustic frequency, are therefore of paramount importance for surface decontamination and their effects depends strongly on the nature and properties of both the contaminant and the surface (Mason, 2016). UNGG Mg materials, through which some long-lived radioisotopes potentially diffused (Hines and Reed, 1966; Hodkin and Mardon, 1965), cannot be significantly decontaminated by a soft sweeping of the surface and the poor corrosion resistance of Mg has therefore to be taken into account (Song and Atrens, 2003). Preliminary studies demonstrated that intermediate acoustic frequencies offer a good compromise between cavitation effect (controlled erosion/dissolution of Mg matrix) and corrosion resistance of Mg (H_2 generation) (Ji et al., 2018).

This article deals with the ultrasound-assisted treatment of extended Mg-based surfaces focusing on UNGG fuel cladding decommissioning. A progressive evaluation of decontamination by acoustic cavitation at 345 kHz is carried out by (i) the study of the behavior of sonicated UNGG cladding and simulant materials (in different shapes: flat disc or cylindrical) in dilute oxalic acid solution, (ii) the contamination of these materials with uranium and their corresponding surface characterization, and (iii) their 345 kHz decontamination regarding both uranium- and carbon-contaminated sides.

2. Experimental

2.1. Materials and solutions

All chemicals and reagents used in this study were of analytical grade and purchased from Sigma-Aldrich (St. Louis, MO, USA). The various solutions were prepared with milli-Q water having a resistivity higher than 18.2 MΩ.cm at 25°C. Mg and Mg/Zr alloy were used as UNGG cladding simulants. Magnesium discs (25 mm diameter and 0.5 mm thickness) and sheets (100 mm x 100 mm, 0.5 mm thickness) were supplied by Goodfellow Cambridge Ltd. (UK) with a 99.9% purity. The sheets were cut into ribbons measuring ca. 45 x 20 mm² before being folded into a cylindrical shape to simulate a complex geometry. Discs of magnesium doped with 0.49 wt.% of zirconium (99.95% purity) were purchased from Neyco (Vanves, France) and were 25 mm in diameter and ca. 1 mm in thickness. The various metallic samples were used as received (without polishing or chemical etching). A genuine but non-irradiated UNGG cladding tube fragment was provided by CEA/DTCD department (Marcoule, France). This cladding fragment was cut into small pieces to obtain smaller samples

exhibiting flat and homogeneous shape in order to be adjusted to the chemical reactor and be representative of the various cladding areas studied. Uranium solutions were prepared by dissolution of $UO_2(NO_3)_2$,6 H_2O salt (CETAMA, France) in pure water. The used uranium was natural with an isotopic composition of 99.27 at.% ^{238}U, 0.72 at.% ^{235}U and 0.005 at.% ^{234}U.

2.2. Contamination of Mg-based materials

Mg-based materials were contaminated by the homogeneous deposition of fine droplets (10 µL) of 0.1 M $UO_2(NO_3)_2$ aqueous solution with a total volume of deposited solution of about 50-70 µL (approx. 1.2-1.7 mg of uranium). After contamination, the samples were left to dry in a fume hood for 12 h before being fired in a tubular oven at 500 °C for 2 h under Ar gas flow (heating rate of 10 °C.min^{-1}). **Fig. 1** shows the example of a Mg/Zr disc contaminated with 70 µL of 0.1 M $UO_2(NO_3)_2$. Preliminary studies demonstrated that higher volumes or concentrations of uranium solution induced droplet coalescence and a poor quality of contamination (not homogeneous and poorly fixed on the matrix, but also giving inaccurate measurements regarding alpha spectrometry results). Mg ribbons were contaminated according to a similar procedure with the deposition of only 30-50 µL of $UO_2(NO_3)_2$ that were uniformly and linearly distributed along the entire length of the sample (3-5 x 10 µL; approx. 0.7-1.2 mg of uranium).

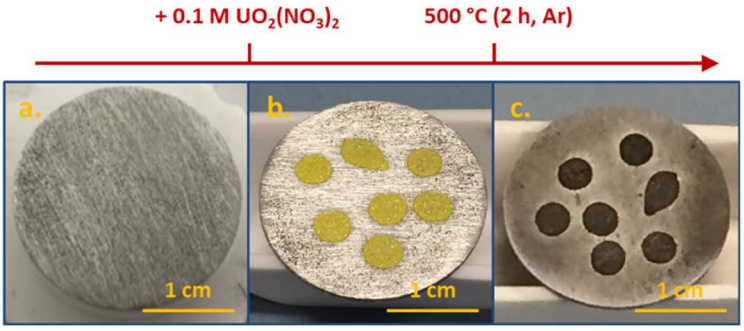

Fig. 1. Contamination procedure of Mg-based materials. The example is given for a 2.5 cm diameter disc of Mg/Zr alloy (a.) on which 70 µL of 0.1 M $UO_2(NO_3)_2$ solution were added (b.) before it was fired at 500 °C during 2 h under Ar gas flow (c.).

2.3. Experimental set-ups

Sonication was performed in a home-made thermostated batch reactor containing 250 mL of solution. The cylindrical reactor was mounted on top of a piezoelectric Elac Nautik (25 cm², Wärtsilä ELAC Nautik GmbH) transducer supplying ultrasound at 345 kHz and powered by a 300 W generator at full capacity (T&C Power Conversion, Inc., Rochester, USA). A machined Teflon lid was placed on top of the reactor. A Teflon bar penetrated the lid to maintain the sample in the reactor at reproducible distance from the transducer (ca. 6 cm). The sample holder consisted in a flat Teflon disc on which Mg-based samples were fixed with microscopy carbon tabs and which was finally screwed on the Teflon bar (Ji et al., 2018). Additional agitation (200 revolution per minute or rpm, i.e. 3.34 Hz) of the Teflon bar was provided by an external motor (VWR VOS 14 Agitator, France) to avoid the accumulation of bubbles at the sample surface that would cushion cavitation and homogenize the solution. The entire device was equipped with Teflon screws, rings and fixings to ensure that the system was tightly sealed. The cylindrical reactor was supplied with side inlets allowing the sampling of the sonicated solution through a septum. The temperature of the solution was controlled during the experiment using a thermocouple immersed in the solution and a

cryostat that maintained the sonicated solution at 18 ± 2°C using an EtOH:H_2O (40:60, v:v) mixture circulating in the cell walls. The acoustic power density P_{ac} ($W.mL^{-1}$) transmitted to the solution was measured by calorimetry as previously described (Dalodière et al., 2016; Virot et al., 2010). The solutions were sonicated at 0.07 $W.mL^{-1}$ and were sparged and saturated with Ar gas (100 $mL.min^{-1}$, provided by Air Liquide, France, 99.9999% purity).

2.4. Characterizations

Inductively coupled plasma-optical emission spectroscopy (ICP-OES). The dissolution of Mg-based materials was evaluated with ICP-OES (Spectro Analytical Instruments GmbH, Germany, equipped for axial plasma observations). During the experiments, aliquots of 1.5 mL were taken at regular time intervals and diluted to the appropriate concentration with 0.3 M HNO_3 prior to analyses. The sample concentration was obtained against an external calibration curve previously prepared in 0.5 M HNO_3 in the 0.5-15 $mg.L^{-1}$ range. The dissolution kinetics (W_t) were obtained by fitting with a linear regression in the 30-60 min sonication range.

Mass spectrometry (MS). During sonication, the generation of H_2 gas was followed with a Thermo Scientific (Prima BT, Thermo Scientific, Waltham, MA, USA) scanning magnetic-sector mass spectrometer tightly connected to the reactor. Molecular sieves (Aldrich, 3 Å) were inserted between the reactor gas outlet and the MS to trap water vapor. H_2 concentration was continuously measured during the experiment with a stable Ar vector flow of 100 $mL.min^{-1}$ (also required to enhance cavitation efficiency); the results were given against an external calibration curve previously obtained with the measurement of H_2/Ar gas mixture standards provided by Air Liquide.

Contact angle measurements. Contact angles were measured on Mg-based surfaces to evidence surface energy differences using a Drop Shape Analyzer (DSA100S, KRÜSS, Hamburg, Germany) by depositing 5 µL sessile droplets (n>8) of pure water with an automated syringe situated on top of the surface. A camera was used to acquire an image for each droplet that was analyzed by a software fitting the drop shape with a geometrical model. The contact angle (θ_i) was given by the angle created between the calculated drop shape function (shape line) and the sample surface (baseline). The provided contact angle ($\overline{\theta}$) was an average value resulting from all the sessile droplets deposited onto the surface in agreement with the equation (**Eq. 2**).

$$\overline{\theta} = \frac{\sum_{i=1}^{n} \theta_i}{n} \qquad \textbf{(2)}$$

Scanning Electron Microscopy (SEM). The evolution of the surface morphology of the studied materials was evaluated with a VEGA3 SEM (Tescan Analytics, France). A Quanta 200 environmental SEM was used for some characterizations to obtain a better resolution and acquire tilted images. Tilted images obtained at the eucentric point (-15°, -10°, 0°, +10°, +15°) were used to reconstruct 3D surfaces with MeX software package (Alicona, Austria) as described in previous investigations (Ji et al., 2018). The reconstructed images gave access to surface roughness (R_a as the average roughness of profile and R_z the mean peak to valley height of roughness profile) and mass loss (ΔM) evolutions. Energy Dispersive X-ray

Spectroscopy (EDX, Bruker XFlash® 5010 SDD, XXX) was coupled to SEM to evaluate the chemical composition (concentration and distribution) of some selected sample areas.

Attenuated Total Reflectance-Fourier Transform Infrared Spectroscopy (ATR-FTIR). ATR-FTIR spectra were acquired between 380 and 4000 cm^{-1} using a PerkinElmer Spectrum 100 (XXX). An average of 8 acquisitions was made for each sample without any specific treatment or preparation.

Alpha spectrometry. The surface radioactive contamination was evaluated by measuring at a reproducible distance the sample α-activity (Becquerel per sample) using a Canberra α-spectrometer (Model 7401, Canberra, France). Spectra were analyzed with Genie 2000 software. Since α-radiation deals with the detection of charged He^{2+} particles easily stopped in air or in the sample thickness, a preliminary study was dedicated to the preparation of the contaminated samples. It showed that a too high concentration or mass of uranium deposited at surface did not provide accurate results (not reproducible contamination, unfixed contamination, thickness of the contamination, superposition of isotope peaks on the energy spectra, etc.). The efficiency of decontamination was evaluated with the decontamination factor (DF) defined in **Eq. 3**. For the initial contaminated sample, and despite the visual good quality and selected conditions, auto-absorption was found to sometimes lead to a measured activity lower than the theoretical dropped off one ($A_{natural\ uranium}$= 25.767 $Bq.mg^{-1}$). As a consequence, some calculated DF may therefore be slightly underestimated.

$$DF = \frac{initial\ activity}{residual\ activity} \qquad \textbf{(3)}$$

3. Results and discussion

3.1. Selection of the parameters, characterization of the native materials and preliminary studies

Mg-based materials were sonicated under ultrasound at 345 kHz in a dilute oxalic acid solution. As described in the introduction, the ultrasonic frequency of 345 kHz provides an intermediate effect for cleaning applications responding to both acoustic cavitation and Megasonic effects. Indeed, this frequency seems ideal compared to the strong and heterogeneous effects provided by low frequency ultrasound (20 kHz) and the softer conditions provided by high frequency ultrasound (1 MHz), resulting in a controlled generation of H_2 gas. The two opposite effects observed in oxalic medium are illustrated in **Fig. S1** (**SI**).(Ji et al., 2018) Furthermore, 345 kHz ultrasound was chosen for the current study given the interesting fundamental results reported at 200 kHz with pure Mg (Ji et al., 2018). Preliminary studies have shown comparable structuring and dissolution effects at Mg surface for experiments carried out at 200 and 345 kHz in oxalic acid solution. Oxalic acid solution is a medium of choice for the decontamination of such materials as this acid is widely used in nuclear industry because of the strong complexes it forms with actinides and their application in the preparation of actinide oxide precursors needed for nuclear oxide fuel preparation (Bonato et al., 2020; Gokulakrishnan et al., 2010; Tyrpekl et al., 2015). It must be noted that water alone is not effective for such decontamination; furthermore, oxalic medium has been widely used (alone or in a mixture) for the decontamination of metal wastes in nuclear site decommissioning (Gokulakrishnan et al., 2010; Kaul and Becker, 2005; L. Chen et al., 1997; Morris, 2011).

The choice of oxalic acid concentration for the preparation of the decontamination solutions was a compromise resulting from preliminary experiments. A weaker effect was observed in our conditions for dilute oxalic acid solutions (e.g. 10^{-3} M) while strong effects were observed at 5 10^{-2} M on the Mg surface with an additional precipitation of Mg oxalate in the system which may hinder the decontamination process and provide cloudy solutions. Concerning the studied material, it is worth noting that the intrinsic properties of Mg coupled with its low neutron capture cross-section forced this element to be considered as a good candidate for nuclear fuel claddings (which is the first barrier against radioactive element dissemination). Its alloying with Zr in good proportion refines the material grain size and decreases the microporosity thus improving the casting quality and mechanical property of the material without disturbing its neutron cross-section (Caillat et al., 1963; Gandel et al., 2016; Song and StJohn, 2002). As Mg alloying with Zr is known to modify the corrosion resistance and microstructure of the material (Gandel et al., 2014; Gandel et al., 2016; Zeng et al., 2018), the first stage of study focused on comparing the behaviour of Mg and Mg-Zr alloy under sonication at 345 kHz before investigating genuine UNGG claddings.

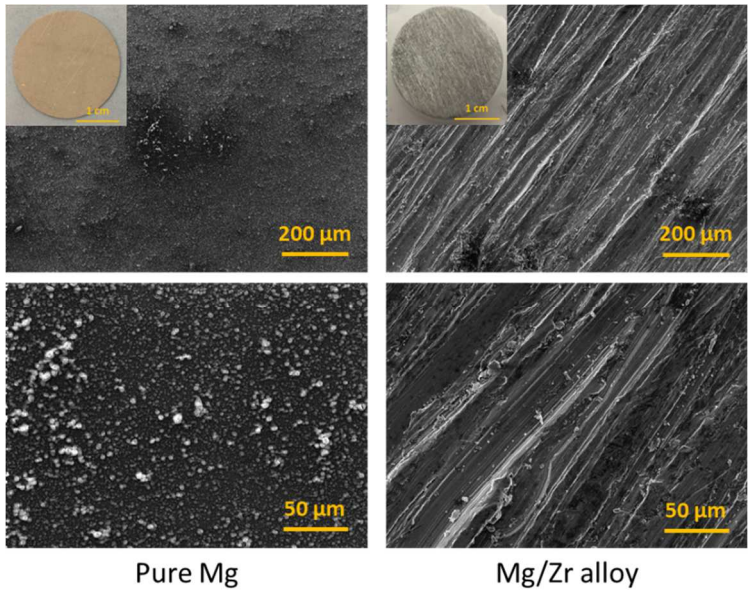

Fig. 2. Optical and SEM pictures acquired on pure Mg and Mg/Zr alloy surfaces.

Fig. 2 compares optical and SEM pictures of untreated Mg and Mg/Zr alloy discs. The native Mg/Zr alloy material had a silver-like color indicating a lower surface oxidation compared to pure Mg (Ji et al., 2018). This claim is confirmed by SEM observations which further showed the formation of a homogeneous distribution of surface oriented linear scratches attributed to the material processing. EDX analyses collected in **Table 1** confirmed that the native Mg/Zr sample exhibits a much lower oxygen content, which corresponds to its apparently lower degree of oxidation. This observation is consistent with several studies that demonstrated the potential increased corrosion resistance of Mg once alloyed with zirconium element in good proportions (Gandel et al., 2014; Gandel et al., 2016; Song and StJohn, 2002). Note that air storage of the as-received materials can also be a variable parameter responsible for surface oxidation of several nanometers (also highly dependent of the humidity) (Fotea et al., 2006; Ogawa et al., 2011). It is interesting to note that Zr was hardly detected in the native Mg/Zr sample due to its low concentration in the material

(0.49 wt.%). Note that both native samples showed detectable amount of carbon up to 15.8 wt.% for Mg and 1.5 wt.% for Mg/Zr alloy. Mg is highly reactive and reacts with oxygen, water, carbon dioxide and volatile species from the air atmosphere (Fotea et al., 2006; Ogawa et al., 2011). As a result, a film composed of a mixture of MgO, $Mg(OH)_2$ and $MgCO_3$ can form at the material surface in addition to volatile organics that can also vary with time as a result of catalytic reaction at the surface (Fotea et al., 2006; Ogawa et al., 2011).

Table 1. Chemical composition (wt.%) of the Mg-based materials determined by EDX spectroscopy

Sample	Mg	Zr	O	C
Native Mg	39.7 ± 3.6	-	44.5 ± 5.2	15.8 ± 2.7
Native Mg/Zr	85.3 ± 4.6	tr.	13.2 ± 2.0	1.5 ± 0.3
Sonicated Mg/Zr – area 1	31.3 ± 2.7	2.4 ± 0.3	59.3 ± 4.4	7.0 ± 0.5
Sonicated Mg/Zr – area 2	80.7 ± 5.6	0.8 ± 0.1	13.5 ± 2.1	5.0 ± 0.5
UNGG cladding (outside), average	62.5 ± 12.7	0.4 ± 0.4	22.3 ± 15.0	14.8 ± 2.6
*UNGG, dark zones**	99.9 ± 0.02	tr.	-	-
*UNGG, bright zones**	97.2 ± 0.4	2.8 ± 0.4	-	-
UNGG cladding (inside, carbon areas)	4.3 ± 0.5	-	22.2 ± 1.1	63.4 ± 8.2

* only Mg and Zr were considered in the measurement. tr.: traces, below the limit of quantification

Fig. 3 shows both the external and internal sides of a genuine UNGG cladding tube fragment investigated in this study: the external fins, historically used to enhance the cooling of the cladding by circulating CO_2 and the internal part, where a graphite coating (referred to as "aquadag") was used to prevent radionuclides diffusion into the Mg matrix, are clearly observed. SEM images (**Fig. 3**) demonstrated that the outside part of the cladding displayed two distinct grey levels with bright and darker areas. The bright zones showed a local Zr enrichment up to approx. 3 wt.% while the surrounding darker areas showed traces of Zr not concentrated enough to be quantified (note, a wt.% composition of approx. 0.5% Zr, 99.49% Mg and 0.016% Mn has been referenced for UNGG claddings in the literature by Lambertin et al. (2012)). These elongated bright zones can be attributed to the precipitation of metastable Mg-Zr solid solutions or particle clusters that were formed during the fabrication process as a result of the low solubility of Zr in Mg (Brady et al., 2017; Ma et al., 2002; Wang et al., 2014). The observed high amount of oxygen and carbon in these UNGG cladding samples indicated a complex oxidation layer similar to that observed on disc simulants. Also note that carbon detection may arise from exfoliated graphite particles from the internal side of the cladding (see below).

SEM observations of the inner part confirmed the presence of a rough surface covered with heterogeneously distributed black particles. More than 60 wt.% of carbon was detected with EDX for the black areas while grey areas, probably resulting from the peeling off of graphite coating, showed a carbon content of approx. 30 wt.% with approx. 50 wt.% of oxygen content. Raman spectrum of the inner part of the claddings (**Fig. S2**, **ESI**) showed vibration bands located at 1580 cm^{-1} and 1350 cm^{-1} which refer to crystalline graphite (G) and crystalline defects (D, or disorder), respectively (Bera et al., 2018; Cançado et al., 2006). The ratio of both D and G band intensities indicated a degree of disorder in graphite crystals which is known to be inversely proportional to the average graphite crystalline size L_a according to the following equation **Eq. 4**. An approximate value of carbon particle size on the UNGG cladding inner side of about L_a= 14.5 nm was hence determined (Cançado et al., 2006).

$$L_a = 2.4 \times 10^{-10} \times \lambda_{laser}^4 \times I_G/I_D \quad (4)$$

Where, λ_{laser} is the wavelength of the incident laser beam (532 nm), I_G and I_D are the respective intensities of both D and G bands ($I_G/I_D = 0.754$).

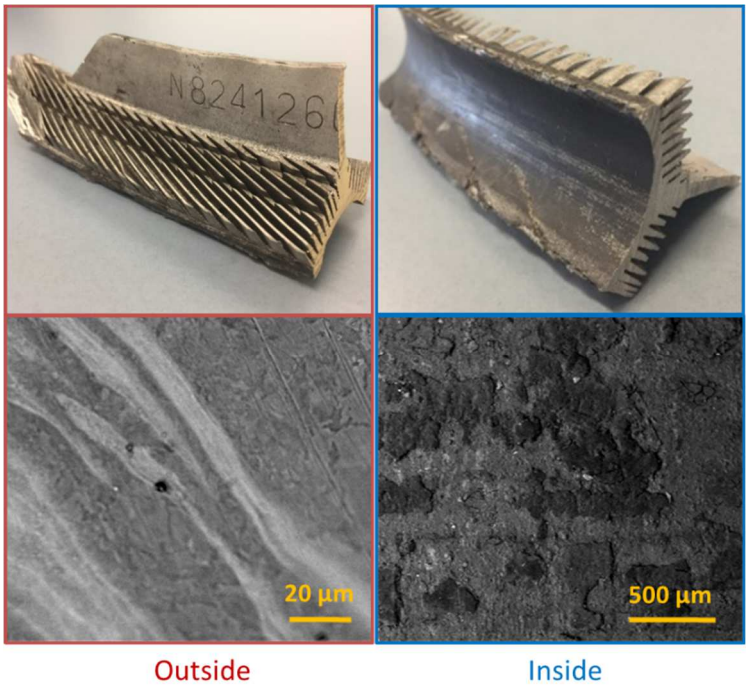

Fig. 3. Picture of the genuine UNGG cladding showing the fins on the outside (left) and the carbon layer referred to as "aquadag" on the inside (right). The geometric complexity of the material to be treated is clearly illustrated and supported with the SEM characterizations at the bottom.

Figures S2, **S3** and **S4** (**SI**) combines Raman, XRD and FTIR characterizations acquired on the various native samples studied in this work. XRD patterns (**Fig. S3**, **SI**) demonstrated the Mg-based composition of the cladding fins (outside region). Some diffraction peaks allowed the identification of MgO and $Mg(OH)_2$ phases (JCPDS 01-080-4185 and 01-078-3952, respectively). Their low intensity confirmed the low oxidation state of the surface despite the storage of UNGG cladding in air atmosphere during several decades agreeing with **Table 1**. Such observation can be attributed to its alloying with Zr which increases the corrosion resistance of the material. However, the high level of Zr and its heterogeneous distribution in Mg-based alloys have been reported to possibly increase the corrosion rate of the material (Gandel et al., 2014). Such observation may explain the intermediate oxidation level noticed for UNGG cladding when compared to pure Mg and Mg/Zr alloy disc samples. Conversely, the inner part of the cladding was found out to be mostly covered by carbon and magnesium hydroxides in agreement with EDX investigations (**Table 1**). Traces of Mg (JCPDS 01-089-5003) were most probably observed as a result of carbon coating flaking off. The strong contribution of $Mg(OH)_2$ diffraction peaks (in opposition to the outside) can be attributed to galvanic corrosion between electrical couples of graphite and exposed substrate of Mg on the internal surface (Lambertin et al., 2016; Rooses et al., 2013). IRTF spectra (**Fig. S4**, **SI**) were consistent with XRD and EDX analyses suggesting that the surface oxidation state of UNGG cladding fins was intermediate between those found for pure Mg

and Mg/Zr alloy. In addition to hydroxyl vibration bands, the fin side also displayed bands attributed to Mg-O, Mg-O-C and organic groups (C-O, C=O and C-O-C). The carbon signature was also highlighted by IRTF on the inner side.

In general, this research revealed strong similarities between the various Mg-based materials investigated in this study and supported the use of Mg and Mg/Zr as simulating materials to investigate the behaviour of genuine UNGG claddings. Despite the roughness of the native materials, the main differences were related to the nature and thickness of the oxidation layer standing at the surface (presence of MgO and $Mg(OH)_2$). Alloying Mg material with Zr was confirmed to offer a better corrosion resistance than pure Mg. The presence of carbon on the inner surface of the material is important and has to be considered beyond radionuclide contamination, as galvanic corrosion and the consequent increase of H_2 generation is an essential parameter to be taken into account during storage.

3.2. Effect of sonication: Mg vs. Mg/Zr

The significant dissolution of Mg/Zr alloy sonicated at 345 kHz in 0.01 M oxalic acid solution was demonstrated with the kinetics provided in **Fig. 4.a**. Mg accumulation curve exhibited different features in agreement with the general mechanism previously discussed by Ji et al. (2018). During the ultrasound-assisted structuring of pure Mg material (200 kHz): (i) a synergistic effect combining the effect of stirring and 345 kHz cavitation was initially observed when comparing the first 30 min of treatment (only stirring) with the rest of the experiment (stirring and ultrasound). (ii) a slow decrease of the Mg accumulation rate was then observed with the sonication time, this behavior can be explained by the consumption of protons from the medium (**Eq. 5**). This phenomenon was confirmed with further addition of oxalic acid (+ 5 10^{-3} M in solution) after 180 min of sonication. (iii) the dissolution of Mg/Zr alloy was finally accompanied by the generation of H_2 gas which followed exactly the kinetics of the different period observed on the dissolution curve. It is however important to note that the amount of H_2 gas released was not equal the amount of Mg determined in solution. Such non-stoichiometry has already been observed by other authors and attributed to the diffusion of H_2 gas into the Mg matrix (Ding et al., 2017; Edalati et al., 2016; Ji et al., 2018; Nogita et al., 2009; Zainal Abidin et al., 2011). The influence of H_2 during treatment is not really clear at the moment and will require further investigation. Nevertheless, we suggest that in our gas conditions H_2 is not troubling the treatment due to the low amount generated.

$$Mg + 2\ H^+ \rightarrow Mg^{2+} + H_2 \qquad (5)$$

Fig 4.b. presents the dissolution kinetics of Mg/Zr alloy and UNGG cladding (the latter will be discussed in the following section) materials sonicated at 345 kHz in 0.01 M oxalic acid solution. It focuses on the initial dissolution period. The dissolution curves presented, demonstrate again the significant effect of 345 kHz ultrasound (combined with 100 rpm stirring, i.e. 1.67 Hz) in comparison to sole stirring regardless of the studied material. For Mg/Zr alloy, it is interesting to note that the dissolution was not linear in the initial part (first 10 min) and showed a dissolution jump which could be attributed to a quick dissolution and solubilization of the surface defects under ultrasound. The residual dissolution then appeared linear in the 30-60 min range. The normalized dissolution rates are gathered in **Table 2** and compared to those obtained for pure Mg (and UNGG cladding) under stirring

and sonication in similar conditions. The linear rates (in this experimental domain) demonstrated similar results for pure Mg sonicated at 200 or 345 kHz suggesting the relevant comparison of the current study with the previous results (Ji et al., 2018). The normalization of the 345 kHz dissolution rates with the exposed surface area and the materials density provided a dissolution rate of 0.54 µm.min^{-1} for pure Mg against 0.51 for Mg/Zr alloy in agreement with an increased corrosion-resistance reported for Mg-based alloys by Zeng et al. (2018).

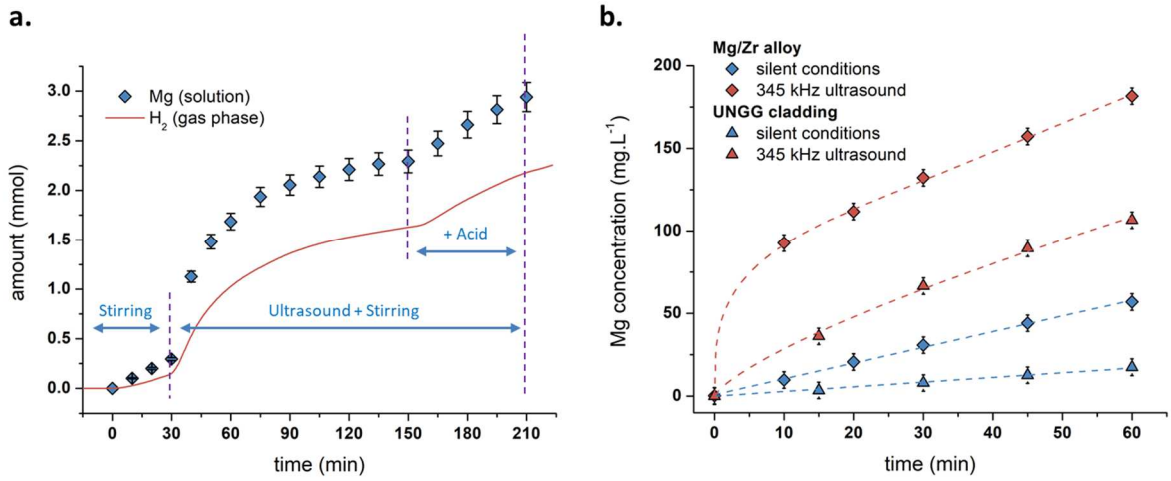

Fig. 4. (a.) Cumulative amounts (mmol) of Mg and H_2 observed in the liquid and gaseous phases, respectively, observed during sonication at 345 kHz of a Mg/Zr alloy in 0.01 M oxalic acid solution (P_{ac}= 40 W, 20°C, 250 mL, 100 rpm). Dissolution started by stirring for 30 min without ultrasound. Additional sonication started at t= 30 min and addition of oxalic acid up to 0.1 M was performed at t= 150 min.(b.) Mg accumulation kinetics observed during the stirring or sonication (345 kHz, P_{ac}= 40 W, 20°C, 100 rpm) of Mg/Zr alloy and genuine UNGG cladding in 0.01 M oxalic acid solution.

Table 2. Normalized dissolution rates observed during the 345 kHz sonication of Mg, Mg/Zr and UNGG cladding materials (Ar, 20°C, 100 rpm) in 0.01 M oxalic acid solution.

Sample *Conditions*	**W_t(Mg)** **(mg.L^{-1}.min^{-1})**	**R_L** **(mg.cm^{-2}.min^{-1})**	**R_T** **(µm.min^{-1})**
Mg			
US (200 kHz) + stirring (100 rpm) (Ji et al., 2018)	1.76	0.09	0.52
US (345 kHz) + stirring (100 rpm)	1.83	0.09	0.54
Mg/Zr alloy			
US (345 kHz) + stirring (100 rpm)	1.73	0.09	0.51
Stirring (100 rpm)	0.90	0.05	0.26
UNGG cladding			
US (345 kHz) + stirring (100 rpm)	1.54	0.26	1.47
Stirring (100 rpm)	0.28	0.05	0.27

Indicated dissolution rates were calculated using a sonicated surface of S= 1.5 cm^2 for UNGG cladding fins and 4.9 cm^2 for the disc simulants and a material density of ρ= 1.738 g.cm^{-3}. US= ultrasound. R_L is the dissolution rate normalized with the sonicated surface area whereas R_T also takes into account the material' density. Uncertainty is lower than 5%.

Fig. 5 compares Mg-Zr alloy sample before and after 345 kHz sonication in 0.01 M oxalic acid (P_{ac}= 40 W, 20°C, 100 rpm). After 60 min, a homogeneous and bright metallic surface was

observed. Surface modifications were visible to naked eye and were later confirmed with SEM images which revealed a homogenous distribution of 30-40 µm diameter craters in agreement with the recent "golf ball" shape structuration noticed during the sonication of pure Mg (enlarged picture of sonicated Mg/Zr alloy with a lower magnification is provided in **Fig. S5, ESI**). 3D reconstruction of the surfaces (**Fig. 5**) and the corresponding extracted parameters gathered in **Table 3** show that the native Mg/Zr surface exhibited a much higher roughness (R_a= 271 nm and R_z= 1.31 µm) than what previously observed for pure Mg (R_a= 61 nm and R_z= 328 nm) by Ji et al. (2018). The corresponding water contact angle analysis of Mg/Zr alloy revealed a smaller value (81 ± 3°) than that measured for pure Mg (120 ± 4°), such difference can be related to surface heterogeneities and oxidation film differences. After sonication, the ultrasound-assisted formation of craters lead to a much higher roughness on Mg/Zr sample despite their relative similar sizes (R_a= 371 nm and R_z= 1.79 µm against R_a= 212 nm and R_z= 606 nm for pure Mg).

Table 3. Determined parameters for Mg, Mg/Zr and UNGG cladding samples treated under stirring with or without ultrasound during 60 min in 0.01 M oxalic acid solution at 345 kHz (P_{ac}= 40 W) under Ar (100 mL.min^{-1}).

Sample Surface	Original surface			Sonicated surface				Surface after stirring		
	R_a (nm)	R_z (nm)	CA (°)	R_a (nm)	R_z (nm)	CA (°)	Crater (µm)	R_a (nm)	R_z (nm)	CA (°)
Pure Mg	61	328	120	212	606	100	40	44	260	61
Mg/Zr alloy	271	1310	81	371	1790	108	30-40	-	-	83
UNGG (fins)	-	-	-	501*	2180*	-	20-40	334	1720	-

*values given as a global measurement (craters: R_a= 907.7 nm, R_z= 1.65 µm and undulations: R_a= 106.2 nm, and R_z= 0.30 µm). Uncertainty on the given values is estimated to be about 5%.

The evolution of the surface tension for Mg/Zr alloy during sonication (and more generally, throughout dissolution) could be slowed down by decreasing the oxalic acid concentration. This approach allowed demonstrating that the water contact angle decreased rapidly within the first 10 min of sonication until it reached a minimum of ca. 45° (**Fig. S6, ESI**). As proven in the inset pictures, this behavior was concomitant with the removal of surface defects and formation of crater nuclei, which was maintained during approx. 60 min. The contact angle then increased strongly while craters were formed and homogeneously distributed at the sample surface. According to Cassie–Baxter model, a higher roughness brings a larger contact angle, which is consistent with the difference observed between the sonicated Mg (about 100°) and Mg-Zr surfaces (about 108°). This evolution trend once again confirms the strong correlation between the formation of craters and surface wettability. The observed differences between Mg and Mg/Zr samples may be attributed to initial surface scratches and defects that may act as nuclei for cavitation and starting sites of electrochemical corrosion and therefore accelerate the formation of crater structures on Mg-Zr surfaces.

Previous investigations carried out on pure Mg evidenced the formation of neo-formed phases and attributed this phenomenon to the formation of $Mg(OH)_2$ accumulating along with Mg dissolution (Ji et al., 2018). Sonication of Mg/Zr alloy has also led to the observation of secondary phases with different sizes and shapes as shown in **Fig. 6**. Large aggregates of more than 100 µm were observed (area 1) around poorly structured regions, while areas with a high concentration of craters (area 2) showed the presence of spherical particles of smaller size (less than 10 µm in diameter). The poor structuration observed around large aggregates suggested that the formation of craters results from a supported formation mechanism in which ultrasound generation of defects (but also the resulting generation of

hydrogen gas) could serve as nuclei for the formation of new acoustic bubbles that implode near their formation site. On the other hand, the precipitation of secondary phases obviously concentrated on certain areas on the surface.

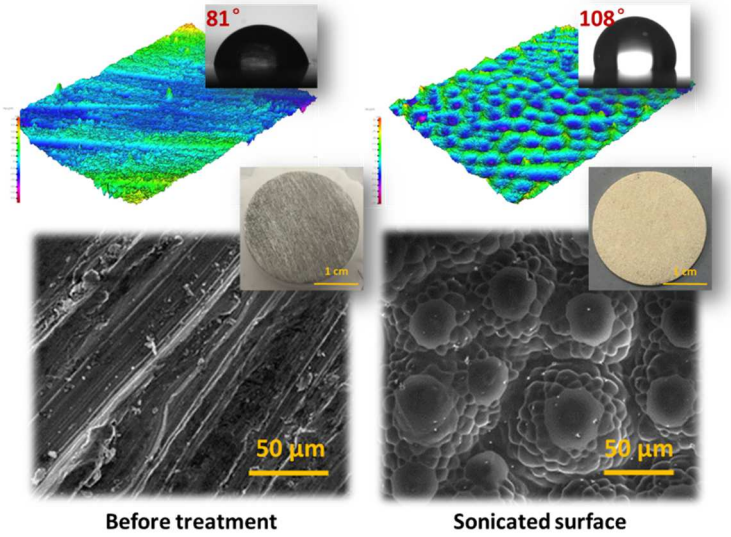

Fig. 5. SEM observations of Mg/Zr alloy sample before and after 345 kHz sonication during 60 min in 0.01 M oxalic acid solution (Ar, 20°C, P_{ac}= 40 W). Corresponding sample disc pictures, 3D MEX reconstructions and water contact angle measurements are also provided.

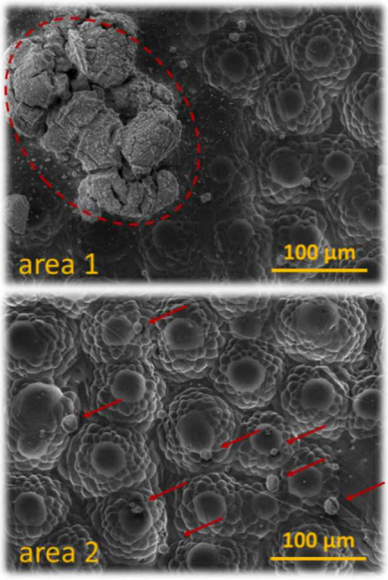

Fig. 6. SEM observation of the secondary phases on Mg/Zr alloy surface after 345 kHz sonication in 0.01 M oxalic acid solution (Ar, 20°C, P_{ac}= 40 W, 60 min). Red arrows show secondary phases generated during treatment.

EDX characterizations of these secondary phases are provided in **Table 1. It** demonstrates an increased concentration of Zr and C in these regions in comparison to native Mg/Zr samples. While the concentration of Mg and O elements was close to the native surface for area 2, a low amount of Mg and a huge amount of O was observed on the large aggregate in area 1. Due to the strong hydrolysis of zirconium, it is assumed that a solid phase that includes hydroxyl and oxalate ligands may precipitate in slightly acidic conditions including

$Zr(OH)_n(Ox)_{(4-n)/2}$ (with 2<n<4 and Ox= oxalate) compound (Kobayashi et al., 2009a; Kobayashi et al., 2009b). A mixture of $Mg(OH)_2$, $Zr(OH)_4$ and magnesium oxalates could also be a possible hypothesis. Furthermore, localized galvanic corrosion where Zr would act as a cathode and Mg as an anode, could involve the precipitation and accumulation of Mg hydroxides and oxides at the cathode site where enrichment with Zr takes place (Chartier et al., 2017). For instance, Gandel et al. (2016) demonstrated that Zr can be considered as an anodic activator of Mg resulting in the increase of the corrosion rate of Mg-based materials. Note also that the exact nature of this phase was difficult to determine since the pH is changing with dissolution progress (due to proton consumption) and may also strongly vary near the surface when Mg dissolves resulting in the precipitation of $Mg(OH)_2$ as a secondary phase.

A primary conclusion reveals that Mg/Zr surface exhibited quite similar properties with pure Mg under 345 kHz ultrasound irradiation in terms of dissolution profile and yields, contact angle evolution and microscale structuring. Significant differences may nevertheless be discussed regarding the roughness values (much higher for Mg/Zr samples) and chemical composition of the generated secondary phases. These two parameters are directly resulting from the contribution of Zr in Mg material and a possible ultrasound-activated galvanic corrosion. Nevertheless, both Mg and Mg/Zr sonochemical structuring behaved similarly at 345 kHz and therefore should help in understanding the potential ultrasound-assisted decontamination of genuine UNGG claddings in such conditions.

3.3. Structuring effect on UNGG cladding fragments

The dissolution rate (W_t(Mg) in $mg.L^{-1}.min^{-1}$) observed for UNGG cladding sample in similar conditions (**Fig. 4.b.**) was slightly lower than that observed with Mg/Zr alloy but was much more important once normalized with its exposed surface and material' density (1.45 $\mu m.min^{-1}$ against 0.51 $\mu m.min^{-1}$, respectively, **Table 2**). Such difference meant that UNGG is more easily dissolved under these conditions in comparison to its simulating materials and also to pure Mg. This observation may result from the sample aging and the strong oxidation of its surface which can be more easily depassivated under ultrasound. In addition, Gandel et al. (2014) reported the increased corrosion rate of Mg alloys containing high level of Zr (above ca. 0.5 wt.%) and not homogenously dispersed Zr particles. The presence of impurities in the matrix is also known to favor detrimental micro-galvanic corrosion in the matrix (Gandel et al., 2014; Song, 2005; Zeng et al., 2006). **Fig. 7** shows the sonication effect observed in 0.01 M oxalic acid solution on fins taken from the outer part of UNGG cladding and compares them with a similar material which was only treated under stirring. It is interesting to note the "golf-ball shape" structuring of UNGG cladding material under 345 kHz in agreement with the results obtained on pure Mg and Mg/Zr alloy. Nevertheless, the corresponding size distribution of the craters and their dispersion at the surface was slightly different from what observed with the other materials (**Fig. 6** or **Fig. S7** compared to **Fig. 7**, for instance). The size of the craters indeed varies between 20 to 50 µm (**Table 3**). They also appear heterogeneously dispersed on the surface and surrounded by small pits forming undulations as observed in **Fig. S7** (**SI**). These two features exhibited a different roughness as described by **Table 3.**

One can assume that the low roughness undulations result from micro- and acoustic streaming that preceded the formation of the craters. In comparison to the other materials,

the formation of these undulations and the heterogeneous surface structuring resulted most probably from the initial surface oxidation but also from the heterogeneous contribution of Zr in the material (**Table 1**). Indeed, Zr addition in Mg alloy has been reported to modify the grain size and improve the ductility of the material by reducing the nucleation, growth and coalescence of cracks and voids at grain boundaries (Sun Fangfang, 2017; Wen et al., 2014). The strong differences noticed at the cladding surface as regard to Zr concentration suggest mechanical and corrosion differences that explain the more heterogeneous structuring of its surface in comparison to simulating materials. By contrast and in agreement with Ji et al. (2018), the UNGG cladding surface treated under silent conditions (100 rpm stirring) did not show surface structuring and dissolution was slower as observed by **Fig. 7** and **Table 2** (the slow surface evolution can be observed in **Fig. S8, SI**) (Ji et al., 2018). The absence of craters and undulations is clearly pointed out, so as the slow removal of magnesium defects and imperfections (also in agreement with the low dissolution kinetics reported in Table 2), which provided lower roughness parameters of 334 nm and 1720 nm.

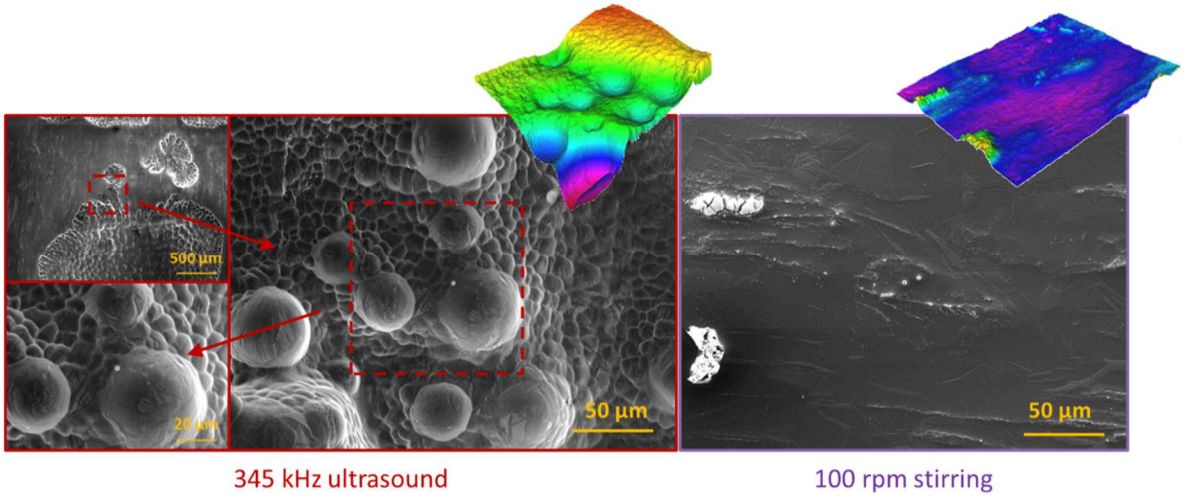

Fig. 7. SEM observations of UNGG cladding (fins) treated during 60 min under 345 kHz ultrasound (left side, P_{ac}= 40 W, 100 rpm stirring, Ar, 20 °C) or silent conditions (right side, 100 rpm stirring, Ar, 20 °C). Inserts show the corresponding 3D MEX reconstructions which allowed to obtain morphologic parameters.

Sonication of the carbon-contaminated UNGG cladding fragment (inner side) has been carried out in similar conditions. **Fig. 8** demonstrates the dramatic effect created by acoustic cavitation after 60 min in 0.01 M oxalic acid solution (20 °C). An important and progressive removal of carbon particles can clearly be observed by the naked eye. After 1 h of sonication, a clean, bright and metallic surface poorly contaminated with residual carbon particles could be observed, a major evidence of the efficiency of the sonochemical treatment. EDX analyses carried out on the bright areas (without visual graphite residues) showed a strong decrease in the amount of carbon to ca. 2 wt.% (>60 wt.% at initial stage). The carbon removal revealed a regular distribution of parallel grooves accompanied with the formation of linearly oriented craters in agreement with observations on other Mg-based materials (**Fig. 8**). The removal of carbon materials revealed the grooves, that are suggested to result from the cladding manufacture and which could acts as nucleation sites for the cavitation bubbles (heterogeneous nucleation). Such hypothesis, explains clearly the parallel distribution of craters on the sonicated surface. The form and size of these craters agreed with the observations made on the other Mg-based materials. Interestingly, we also noticed the formation of secondary phases.

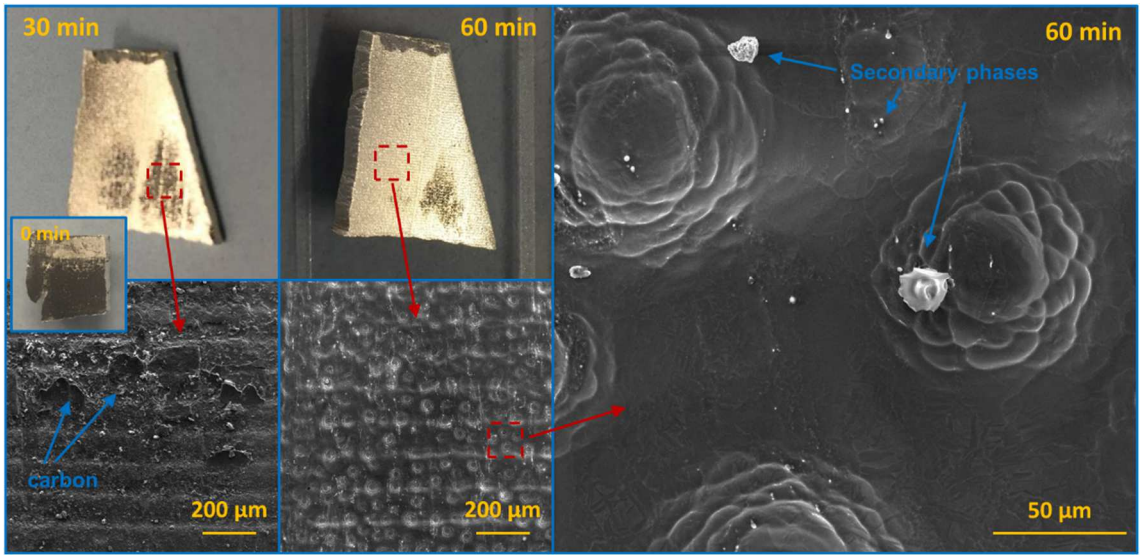

Fig. 8. Picture and SEM observations of the inner side of a UNGG cladding fragment contaminated with carbon before (inset as an example) and after 345 kHz sonication (30 and 60 min) in 0.01 M oxalic acid (Ar, stirring 100 rpm, 20°C, P_{ac}= 40 W).

In general, 345 kHz ultrasound allowed UNGG materials to be structured in a similar way as with other materials. However, the observed heterogeneity and polydispersity can be attributed, most probably, to the surface oxidation and Zr local concentration. Sonication of the inner side of the cladding provided a very simple and efficient route to remove the carbon coating that could lead to galvanic corrosion and the potential generation of hydrogen gas that would interfere with a safety storage.

3.4. Contamination and speciation of uranium at Mg surface

The scheme shown in **Fig. 1** presents the procedure used to contaminate Mg-based samples with uranium. The morphology of the contamination investigated with SEM can be observed in **Fig. 9** for Mg/Zr alloy surface. Uranium contamination appears as 3-5 mm adhering spherical areas, principally composed of large exfoliated flakes ranging from 20 to 500 µm combined to polydispersed particles of micrometric size. EDX spectroscopy confirmed the main composition of the contamination zone to be about 35 wt.% Mg, 26 wt.% O and 39 wt.% U. Nevertheless, a careful comparison of the as-prepared samples in both **Fig. 1** and **Fig. 9** demonstrates significant heterogeneities and differences about the chemical nature of the contaminants. Indeed, different colors going from deep black to orange are clearly observed in **Fig. 9**. Considering the calcination temperature (500 °C), the decomposition of uranyl nitrate solution deposited at the sample surface should form uranium trioxide (UO_3) of orange color according to equation **Eq. 6** (UO_3 can also be yellow or red as a function of the trioxide crystalline phase) as reported by Grenthe et al. (2006) or Sweet et al. (2013). However, UO_3 is not stable at high temperature and can further decompose into U_3O_8 of black color according to the reaction **Eq. 7**. As reported, this transformation is initiated under air at ca. 450°C and remains incomplete until the temperature reaches approx. 650°C (Grenthe et al., 2006).

$$UO_2(NO_3)_2 \xrightarrow{500\,^{\circ}C} UO_3 + 2\,NO_2 + ½\,O_2 \quad (6)$$

$$3UO_3 \xrightarrow{450-650\,^{\circ}C} U_3O_8 + ½\,O_2 \quad (7)$$

One can assume, that such process may be reinforced by the reducing nature of metallic Mg. This hypothesis is further strengthened with the slightly acidic nature of uranyl nitrate solution which visually reacted with the Mg-based surfaces and homogeneized the chemicals during deposition prior to drying and heating. It is expected that a complex contamination composed of UO_3, U_3O_8 and magnesium uranates $Mg_xU_yO_z$ may formed at the surface of the investigated samples. However, it should be noted, that the few studies dealing with $Mg_xU_yO_z$ species have been generally reported at higher temperatures (Fujino, 1972; Fujino and Naito, 1970; Haag and Muncy, 1964; Murthy, 1988; O'Hare et al., 1977; Serizawa et al., 1995). In addition, it is important to emphasize that heterogeneous heating areas in the furnace in addition to oxygen traces could significantly affect the relative proportion and nature of the contaminant species. The visual observation of contamination differences was equally noticed on Mg, Mg/Zr alloy and genuine UNGG cladding (fin side). XRD observations gathered in **Fig. S9** (**SI**), for UNGG cladding as an example, showed several sharp diffraction peaks attributed to Mg matrix in addition to several broad peaks of relatively small intensity that can be assigned to uranium oxide phases (UO_3 or U_3O_8) or magnesium uranates referred to as MgU_3O_{10}.

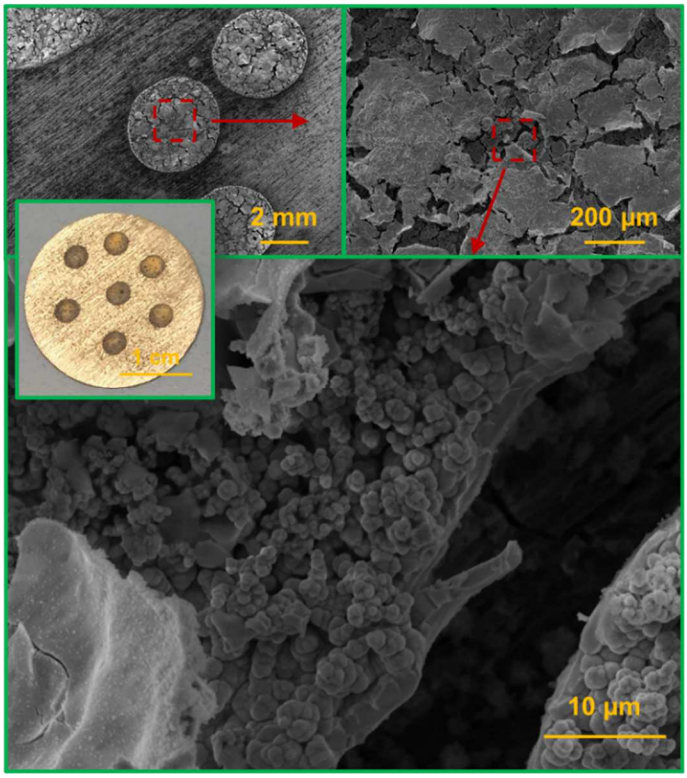

Fig. 9. Picture of Mg/Zr surface contaminated with 0.1 M $UO_2(NO_3)_2$ and fired at 500°C under Ar during 2 h. SEM pictures focus on the contamination part with different magnifications.

Vibrational spectroscopy can be used to specify the crystalline phases dealing with uranium oxides (Desgranges et al., 2012; Elorrieta et al., 2016; Silva et al., 2017). **Fig. 10** combines FTIR and Raman spectroscopies carried out on the orange and black contamination spots of the Mg/Zr disc sample. Several FTIR peaks standing below 2000 cm^{-1} could be assigned to O-H and Mg-O vibrations but also to Mg-O-C, C-O, and possibly C-O-C and C=O vibrations due to the adsorption of CO_2 and volatile organic species, and the presence of carbonates (Bera et al., 2018; Fockaert et al., 2020; Jung et al., 2003). The possible presence of UO_3 and U_3O_8

could be suggested with U-O vibrations in the 1000-500 cm^{-1} region (Allen et al., 1976; Desgranges et al., 2012; Nipruk et al., 2011; Poncet et al., 1999; Silva et al., 2017). Several vibration bands could be assigned to UO_3 and U_3O_8 in Raman spectroscopy in different proportions for both black and orange contaminated areas (**Fig. 10**) (Allen et al., 1987; Ho et al., 2015; Palacios and Taylor, 2000; Wozniak, 2017). In addition, several vibration bands observed on the black contaminated area could refer to non-stoichiometric $Mg_xU_yO_z$ or U_xO_y phases (Allen et al., 1987; Allen and Griffiths, 1979; Elorrieta et al., 2016; Palacios and Taylor, 2000). Not all vibration bands were observed for the studied compounds and they were not exactly located at the positions given in the literature suggesting a complex surface contamination superimposed to magnesium and its oxides. Additional studies are required to better characterize the Mg-based surface contamination.

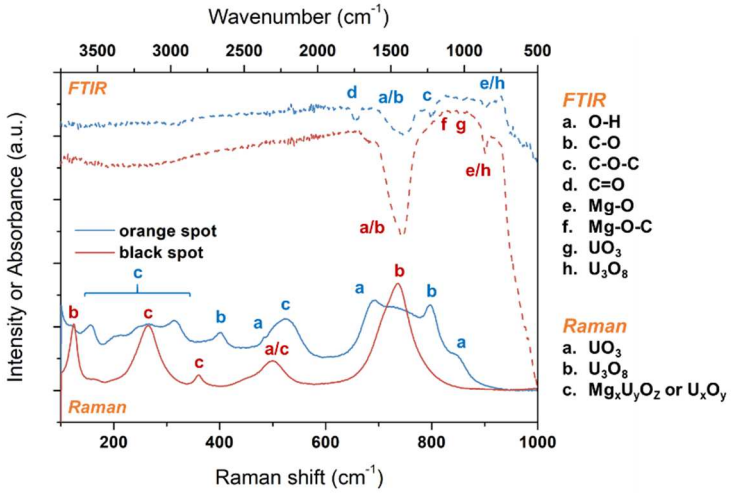

Fig. 10. Raman and FTIR spectroscopy spectra acquired on Mg/Zr samples contaminated with 0.1 M $UO_2(NO_3)_2$.

3.5. Ultrasound-assisted decontamination of UNGG claddings and simulating materials

Fig. 11.a. compares optical and SEM pictures of U-contaminated Mg/Zr alloy discs treated with an in-situ stirring (100 rpm) in 0.01 M oxalic acid solution with and without 345 kHz ultrasound. Residual contamination (dark areas) was observed with the naked eye on the disc treated without ultrasound unlike the sonicated one which exhibited a clean and shiny metallic surface devoid of visual contamination. SEM investigations (**Fig. 11.a.**) confirmed the removal of the uranium contamination on the sonicated Mg/Zr sample and the homogeneous structuring of the surface with the formation of monodispersed craters in agreement with the previous results reported in the current study. The remaining contamination on the stirred sample (silent conditions) was also confirmed with SEM and reached 35 wt.% of uranium for some areas according to EDX measurements. By contrast, the sonicated sample showed at maximum less than 2 wt.% at the initially contaminated spot. Decontamination kinetics, which have been determined with alpha-spectroscopy for both approaches, can be observed in **Fig. 11**. They confirmed the observations made after SEM observation by demonstrating a significant alpha-activity on the stirred sample in opposition to the value obtained for the sonicated sample. The corresponding decontamination factors calculated after 90 min treatment agreed with these observations with DF= 5 for silent conditions and DF= 15 for 345 kHz sonication.

In the studied experimental domain, it is interesting to point out how slow was the decontamination in stirred sample compared to the sonicated sample where

decontamination was nearly instantaneous and required only 20 min of sonication to reach a very low level of alpha-activity at the surface of the sample (A< 1 Bq in 20 min against A= 4.4 Bq after 90 min of sole stirring). Acoustic cavitation phenomenon, which involves the formation of micro-jets, shock waves and micro-streamings at the solid/liquid interface, is known to generate strong diffusion and mass transfer at the interface. These processes may facilitate chemical reactions and mechanical damages including surface depassivation and erosion which significantly enhanced the efficiency and rate of decontamination for Mg/Zr alloy (Moutarlier et al., 2020; Moutarlier et al., 2015; Verdan et al., 2003; Virot et al., 2010; Virot et al., 2012). Reports dealing with nuclear decontamination under ultrasound are particularly scarce in literature (Wells, 1965; Wells, 1966). Nevertheless, decontamination tests have been recently performed on metallic waste samples at Beloyarsk nuclear power plant (Lebedev et al., 2017). The published results demonstrate their significant decontamination in less than 3 h treatment with ultrasound with a high decontamination factor (from ca. 5 to 0.23 $kBq.kg^{-1}$). Lebedev et al. (2017) demonstrated that the decontamination of these samples under conventional conditions requires 110 h and reaches a more modest decontamination efficiency (from ca. 5 to 2.24 $kBq.kg^{-1}$). More recently, Kumar et al. (2014) reported the ultrasonic decontamination of more complex surfaces with the treatment of fast breeder reactor fuel pins using an ultrasonic tank of 4 meter long. A decontamination efficiency higher than 99% has been reported for the treated pin collection.

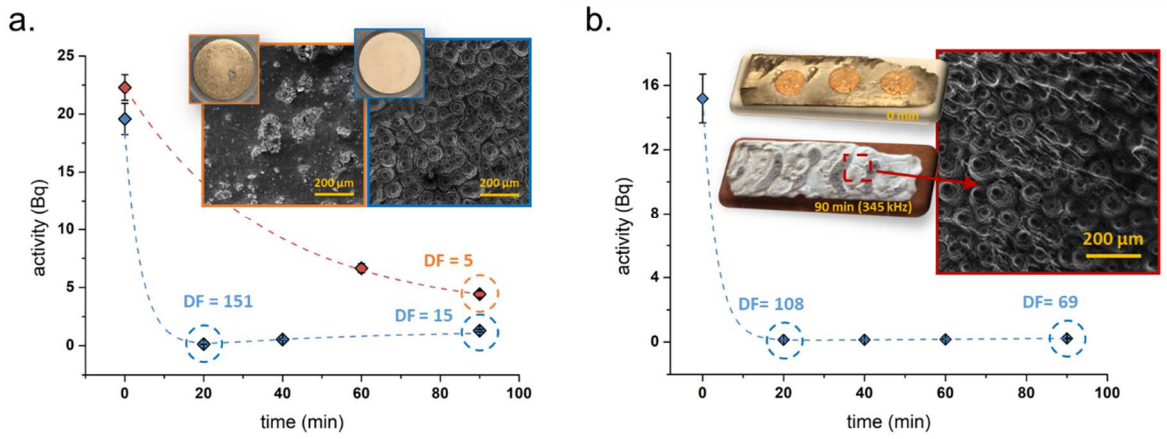

Fig. 11. (a.) Alpha-radioactivity evolution of U-contaminated Mg-Zr surfaces treated in 0.01 M oxalic acid under stirring (100 rpm) with (blue data) and without (red data) ultrasound. Inserts: Optical and SEM pictures of U-contaminated Mg-Zr surfaces. (b.) Ultrasound-assisted decontamination of a fin UNGG fragment. Inserts show optical and SEM pictures of the sample before and after decontamination. Contamination of the samples was carried out with 70 µL (a.) and 30 µL (b.) of 0.1 M $UO_2(NO_3)_2$ solution. Decontamination conditions: 345 kHz, 90 min, Ar, 20°C, 100 rpm, P_{ac}= 40 W.

Complex geometries were simulated by rolling a contaminated sample in a cylinder shape (**Fig. S10**, **SI**) or by contaminating a genuine UNGG fin fragment (**Fig. 11.b**). The 90 min ultrasonic treatment of these samples in 0.01 M oxalic acid solution provided clean and shiny Mg-based samples devoid of any trace of U contamination. The formation of craters was observed on both contaminated surfaces, indicating that the generation or diffusion of acoustically-active bubbles also occurred at the vicinity of these more complex contaminated samples. The corresponding surface activities showed an instant reduction of the surface contamination in ca. 20 to 40 min with decontamination factors reaching values of DF= 7 and DF= 69 after 90 min sonication for Mg and UNGG matrixes, respectively. EDX

measurements confirmed the strong decrease of uranium in the initially contaminated areas. DF values obtained under ultrasound for the different metallic samples could differ by one order of magnitude due to the different morphology and the difficulty of measurements in the alpha chamber for such elongated sample. Also, the lower amount of dropped off contamination for some samples can be taken into account. In addition, such comparative approach became difficult when the surface was almost completely decontaminated (due to the very low remaining activity). Nevertheless, one can note that the decontamination curves provided in **Fig. 11** and **Fig. S10 (SI)** showed a very rapid decontamination under ultrasound when compared to sole stirring. Surprisingly, a slow but continuous increase of the determined surface alpha-radioactivity was also observed for all samples after most of the contamination has been removed. For instance, UNNG cladding sample showed a decontamination factor of 108 after 20 min sonication which decreased to DF= 69 at the end of the experiment (90 min). Similarly, the decontamination factor observed for Mg surface after 40 min was about DF= 70 and decreased to DF= 7 after 150 min sonication. Mg/Zr showed the highest decrease with a DF value of 151 after 20 min decreasing to only 15 after 90 min of sonication.

Close examination of the decontaminated surfaces indicated secondary phases in agreement with Ji et al. (2018), which suggested the local formation of brucite $Mg(OH)_2$ in combination to Zr-based phases (**Fig. 6** or **Fig. 8**). EDX investigations provided in **Fig. S11 (SI)** demonstrated that these phases were associated with a high amount of uranium on the sonicated samples (10 to 20 wt.% of uranium) whereas the surrounding area did not show significant traces of uranium (<2 wt.%). FTIR spectroscopy confirmed the presence of uranyl vibration bands on the surface (**Fig. S12**, **SI**). To confirm a possible decontamination/recontamination process (in opposition to a residual surface contamination meaning a low efficiency of treatment), a non-contaminated Mg surface was sonicated at 345 kHz in 0.01 M oxalic acid solution during 30 min before 70 µL of 0.1 M $UO_2(NO_3)_2$ were injected in the solution that was further sonicated for 30 additional minutes. Such approach allowed the EDX confirmation of surface-enriched uranium areas by more than 15 wt.% that were found to be associated with secondary phases. Due to its layer structure consisting in double planes of OH groups with low cohesion forces, brucite exhibits $Mg(OH)_2$ stacked layers able to efficiently adsorb surrounding cations as demonstrated by Pushkaryova (1999). Wang et al. (2018) demonstrated the very strong affinity of U(VI) with porous magnesium oxide foam (>2500 $mg.g^{-1}$) and attributed this phenomenon to electrostatic interaction between surface hydroxyl groups and U(VI) and its hydrolyzed forms. This adsorption capacity was furthermore observed to be favored in acidic conditions. $Mg(OH)_2$ was also found to be an excellent adsorbent in the nanometric form (Cao et al., 2012; Chen et al., 2014; Maher et al., 2016; Yan et al., 2013; Zhuang et al., 2016). On the other hand, 22-35 kHz ultrasound has been found to enhance the diffusion rate and yields of Cu and Ni cations into brucite (Bochkarev and Pushkareva, 2005; Pushkareva and Bobyleva, 2003).

Therefore, ultrasound-assisted treatment of contaminated Mg-based materials appeared to occur in two successive processes. First, the ultrasound-assisted controlled dissolution of the Mg support was predominant. Ultrasound allowed the rapid (within 20-40 min) and efficient removal of the contaminants adsorbed onto or into the matrix. The parallel formation of brucite as a secondary phase then lead to the second step where metallic cations

(contaminants) were efficiently adsorbed from the solution. Such process could be strengthened by the pH variations in the solution that may impact brucite generation or cation adsorption (Ji et al., 2018; Wang et al., 2018).

5

Conclusion

Ultrasonic cavitation turns out to be one of the simplest and effective techniques designed for the decontamination of Mg-based surfaces polluted with radionuclides. Despite some striking differences attributed to different corrosion resistances (dissolution kinetics, secondary phase compositions, crater sizes and distribution, etc.), the complete decontamination of UNGG claddings and their simulants was rapidly achieved in 0.01 M oxalic acid solutions under 345 kHz ultrasound. Decontamination occurred through the controlled and regulated dissolution of the surface that went with the formation of craters and secondary phases attributed to brucite and/or zirconium-based phases that participated in a slow recontamination process of the surface by re-adsorption of uranyl cations from the solution. The latter recontamination could be avoided by optimizing the duration of treatment. The approach also allowed removing the carbon layer from the cladding inner side that could also interfere with a safety storage because of galvanic corrosion. In general, the sonochemical approach proposed in this study could initiate economic and security benefits through the downgrading of highly radioactive nuclear wastes with a resulting production of decontamination solutions that could enter in a more classical channel already based on the use of oxalic acid. In addition, the decontaminated Mg could be alternatively stored on a safe and more economic surface storage. To go further, the reuse of Mg in nuclear but also civilian industry could then be considered. In addition, the interesting results observed in this study suggest the possible transposition of this approach for the treatment of other metallic surfaces from nuclear industry including Inox materials or Magnox fuel claddings composed of Mg/Al alloy. The application of ultrasound for the decontamination of Mg-based materials in non-nuclear industry tends to be highly encouraging.

Acknowledgements

The authors gratefully acknowledge Sara El Hakim, Célia Gillet, Joseph Lautru, Xavier Le Goff, Renaud Podor, Cyrielle Rey, Sylvain Robert, Victor Trillaud, for help in experiments, characterizations and useful discussions.

References

Allen, G. C., Butler, I. S., Nguyen Anh, T., 1987. Characterisation of uranium oxides by micro-Raman spectroscopy, J. Nucl. Mater. 144, 17-19.

Allen, G. C., Crofts, J. A., Griffiths, A. J., 1976. Infrared spectroscopy of the uranium/oxygen system, J. Nucl. Mater. 62, 273-281.

Allen, G. C., Griffiths, A. J., 1979. Vibrational spectroscopy of alkaline-earth metal uranate compounds, J. Chem. Soc., Dalton Trans. 315-319.

Bera, M., Chandravati, Gupta, P., Maji, P. K., 2018. Facile One-Pot Synthesis of Graphene Oxide by Sonication Assisted Mechanochemical Approach and Its Surface Chemistry, Journal of Nanoscience and Nanotechnology 18, 902-912.

Bochkarev, G. R., Pushkareva, G. I., 2005. Intensification of Sorption Properties of Brucite, Journal of Mining Science 41, 380-384.

Bonato, L., Virot, M., Dalodière, E., Dumas, T., Mesbah, A., Dieste Blanco, O., Wiss, T., Prieur, D., Rossberg, A., Venault, L., Moisy, P., Nikitenko, S. I., 2020. Probing the local structure of nanoscaled actinide oxides: a comparison between PuO_2 and ThO_2 nanoparticles rules out PuO_{2+x} hypothesis, Nanoscale Adv. 2, 214-224.

Brady, M. P., Ievlev, A. V., Fayek, M., Leonard, D. N., Frith, M. G., Meyer, H. M., Ramirez-Cuesta, A. J., Daemen, L. L., Cheng, Y., Guo, W., Poplawsky, J. D., Ovchinnikova, O. S., Thomson, J., Anovitz, L. M., Rother, G., Shin, D., Song, G.-L., Davis, B., 2017. Rapid Diffusion and Nanosegregation of Hydrogen in Magnesium Alloys from Exposure to Water, ACS Applied Materials & Interfaces 9, 38125-38134.

Breeze, P., Chapter 5 - Gas-Cooled Reactors, in: P. Breeze (Ed.) Nuclear Power, Academic Press, 2017, pp. 45-51.

Brems, S., Hauptmann, M., Camerotto, E., Pacco, A., Kim, T. G., Xu, X., Wostyn, K., Mertens, P., De Gendt, S., 2014. Nanoparticle Removal with Megasonics: A Review, Ecs Journal of Solid State Science and Technology 3, N3010-N3015.

Bulat, T. J., 1974. Macrosonics in industry: 3. Ultrasonic cleaning, Ultrasonics 12, 59-68.

Caillat, R., Hérenguel, J., Salesse, M., Stohr, J., 1963. Raisons du choix de l'alliage Mg-Zr pour le gainage des elements combustibles, J. Nucl. Mater. 8, 1-2.

Cançado, L. G., Takai, K., Enoki, T., Endo, M., Kim, Y. A., Mizusaki, H., Jorio, A., Coelho, L. N., Magalhães-Paniago, R., Pimenta, M. A., 2006. General equation for the determination of the crystallite size La of nanographite by Raman spectroscopy, Appl. Phys. Lett. 88, 163106.

Cannes, C., Rodrigues, D., Barré, N., Lambertin, D., Delpech, S., 2019. Reactivity of uranium in geopolymers, confinement matrices proposed to encapsulate MgZr waste, J. Nucl. Mater. 518, 370-379.

Cao, Q., Huang, F., Zhuang, Z., Lin, Z., 2012. A study of the potential application of nano-Mg(OH)2 in adsorbing low concentrations of uranyl tricarbonate from water, Nanoscale 4, 2423-2430.

Chartier, D., Muzeau, B., Stefan, L., Sanchez-Canet, J., Monguillon, C., 2017. Magnesium alloys and graphite wastes encapsulated in cementitious materials: Reduction of galvanic corrosion using alkali hydroxide activated blast furnace slag, J. Hazard. Mater. 326, 197-210.

Chen, Z., Zhuang, Z., Cao, Q., Pan, X., Guan, X., Lin, Z., 2014. Adsorption-Induced Crystallization of U-Rich Nanocrystals on Nano-Mg(OH)2 and the Aqueous Uranyl Enrichment, ACS Applied Materials & Interfaces 6, 1301-1305.

D'Amico, M., Dufaud, O., Latche, J. C., Trelat, S., Perrin, L., 2016. Parametric study of the explosivity of graphite-metals mixtures, Journal of Loss Prevention in the Process Industries 43, 714-720.

Dalodière, E., Virot, M., Moisy, P., Nikitenko, S. I., 2016. Effect of ultrasonic frequency on H_2O_2 sonochemical formation rate in aqueous nitric acid solutions in the presence of oxygen, Ultrason. Sonochem. 29, 198-204.

Desgranges, L., Baldinozzi, G., Simon, P., Guimbretière, G., Canizares, A., 2012. Raman spectrum of U4O9: a new interpretation of damage lines in UO2, J. Raman Spectrosc. 43, 455-458.

Ding, X., Li, Y., Fang, F., Sun, D., Zhang, Q., 2017. Hydrogen-induced magnesium–zirconium interfacial coupling: enabling fast hydrogen sorption at lower temperatures, Journal of Materials Chemistry A 5, 5067-5076.

Edalati, K., Emami, H., Ikeda, Y., Iwaoka, H., Tanaka, I., Akiba, E., Horita, Z., 2016. New nanostructured phases with reversible hydrogen storage capability in immiscible magnesium–zirconium system produced by high-pressure torsion, Acta Mater. 108, 293-303.

Elorrieta, J. M., Bonales, L. J., Rodríguez-Villagra, N., Baonza, V. G., Cobos, J., 2016. A detailed Raman and X-ray study of UO2+x oxides and related structure transitions, Phys. Chem. Chem. Phys. 18, 28209-28216.

Fockaert, L. I., Würger, T., Unbehau, R., Boelen, B., Meißner, R. H., Lamaka, S. V., Zheludkevich, M. L., Terryn, H., Mol, J. M. C., 2020. ATR-FTIR in Kretschmann configuration integrated with

electrochemical cell as in situ interfacial sensitive tool to study corrosion inhibitors for magnesium substrates, Electrochim. Acta 345, 136166.

Fotea, C., Callaway, J., Alexander, M. R., 2006. Characterisation of the surface chemistry of magnesium exposed to the ambient atmosphere, Surf. Interface Anal. 38, 1363-1371.

Fuchs, F. J., 2000. Effective Use of Ultrasonic Cleaning for Pretreatment, AESF SUR/FIN 946-952.

Fuchs, F. J., 19 - Ultrasonic cleaning and washing of surfaces, in: J.A. Gallego-Juárez, K.F. Graff (Eds.) Power Ultrasonics, Woodhead Publishing, Oxford, 2015, pp. 577-609.

Fujino, T., 1972. Studies on cubic magnesium uranate $Mg_yU_{1-y}O_{2+x}$. Structural analysis, J. Inorg. Nucl. Chem. 34, 1563-1574.

Fujino, T., Naito, K., 1970. Studies on cubic magnesium uranate $Mg_yU_{1-x}O_{2+x}$. 1. Phase relations and crystal chemistry, J. Inorg. Nucl. Chem. 32, 627-636.

Gandel, D. S., Easton, M. A., Gibson, M. A., Abbott, T., Birbilis, N., 2014. The influence of zirconium additions on the corrosion of magnesium, Corros. Sci. 81, 27-35.

Gandel, D. S., Easton, M. A., Gibson, M. A., Abbott, T., Birbilis, N., The influence of Mg-Zr master alloy microstructure on the corrosion of Mg, in: N. Hort, S.N. Mathaudhu, N.R. Neelameggham, M. Alderman (Eds.) Magnesium Technology 2013, Springer International Publishing, Cham, 2016, pp. 157-162.

Gokulakrishnan, N., Pandurangan, A., Somanathan, T., Sinha, P. K., 2010. Uptake of decontaminating agent from aqueous solution: a study on adsorption behaviour of oxalic acid over Al-MCM-41 adsorbents, J. Porous Mater. 17, 763-771.

Grenthe, I., Drożdżyński, J., Fujino, T., Buck, E. C., Albrecht-Schmitt, T. E., Wolf, S. F., Uranium, in: L.R. Morss, N.M. Edelstein, J. Fuger (Eds.) The Chemistry of the Actinide and Transactinide Elements, Springer Netherlands, Dordrecht, 2006, pp. 253-698.

Haag, R. M., Muncy, C. R., 1964. Studies in the system $MgUO_3$-$MgUO_4$, J. Am. Ceram. Soc. 47, 34-36.

Hallam, K. R., Minshall, P. C., Heard, P. J., Flewitt, P. E. J., 2016. Corrosion of the alloys Magnox AL80, Magnox ZR55 and pure magnesium in air containing water vapour, Corros. Sci. 112, 347-363.

Hines, G. F., Reed, D., 1966. The assessment of plutonium and fission product distribution in magnox cans from irradiated fuel elements, Journal of Applied Chemistry 16, 90-93.

Ho, D. M. L., Jones, A. E., Goulermas, J. Y., Turner, P., Varga, Z., Fongaro, L., Fanghänel, T., Mayer, K., 2015. Raman spectroscopy of uranium compounds and the use of multivariate analysis for visualization and classification, Forensic Science International 251, 61-68.

Hodkin, D. J., Mardon, P. G., 1965. The diffusion of plutonium in magnesium and magnesium alloys, J. Nucl. Mater. 16, 271-289.

Ji, R., Virot, M., Pflieger, R., Podor, R., Le Goff, X., Nikitenko, S. I., 2018. Controlled "golf ball shape" structuring of Mg surface under acoustic cavitation, Ultrason. Sonochem. 40, 30-40.

Jung, H. S., Lee, J.-K., Kim, J.-Y., Hong, K. S., 2003. Crystallization behaviors of nanosized MgO particles from magnesium alkoxides, J. Colloid Interface Sci. 259, 127-132.

Kaul, A., Becker, D., Radiological Protection, Springer-Verlag Berlin Heidelberg, 2005.

Kobayashi, T., Sasaki, T., Takagi, I., Moriyama, H., 2009a. Solid phase precipitates in (Zr,Th)-OH-(oxalate, malonate) ternary aqueous system, Radiochim. Acta 97, 237-241.

Kobayashi, T., Sasaki, T., Takagi, I., Moriyama, H., 2009b. Zirconium Solubility in Ternary Aqueous System of Zr(IV)-OH-Carboxylates, J Nucl Sci Technol 46, 142-148.

Kumar, A., Bhatt, R. B., Behere, P. G., Afzal, M., 2014. Ultrasonic decontamination of prototype fast breeder reactor fuel pins, Ultrasonics 54, 1052-1056.

L. Chen, D. B. Chamberlain, C. Conner, Vandegrift, G. F., A Survey of Decontamination Processes Applicable to DOE Nuclear Facilities in, Argonne National Laboratory, Argonne, 1997, pp. 1-83.

Lambertin, D., Frizon, F., Bart, F., 2012. Mg–Zr alloy behavior in basic solutions and immobilization in Portland cement and Na-geopolymer with sodium fluoride inhibitor, Surf. Coat. Technol. 206, 4567-4573.

Lambertin, D., Rooses, A., Frizon, F., Galvanic Corrosion of Mg-Zr Alloy and Steel or Graphite in Mineral Binders, in: N. Hort, S.N. Mathaudhu, N.R. Neelameggham, M. Alderman (Eds.) Magnesium Technology 2013, Springer International Publishing, Cham, 2016, pp. 153-155.

Lebedev, O., Lebedev, N., Gavrilov, Y., Doilnitsyn, V., Akatov, A., Development and application of the ultrasonic technologies in nuclear engineering, in: Scientific proceedings III International scientific-Technical conference "Innovations", Paris, France, 2017, pp. 128-132.

Ma, Q., StJohn, D. H., Frost, M. T., 2002. Characteristic zirconium-rich coring structures in Mg–Zr alloys, Scripta Mater. 46, 649-654.

Maher, Z., Ivanov, P., O'Brien, L., Sims, H., Taylor, R. J., Heath, S. L., Livens, F. R., Goddard, D., Kellet, S., Rand, P., Bryan, N. D., 2016. Americium and plutonium association with magnesium hydroxide colloids in alkaline nuclear industry process environments, J. Nucl. Mater. 468, 84-96.

Mason, T. J., 2016. Ultrasonic cleaning: An historical perspective, Ultrason. Sonochem. 29, 519-523.

Mason, T. J., Cobley, A. J., Graves, J. E., Morgan, D., 2011. New evidence for the inverse dependence of mechanical and chemical effects on the frequency of ultrasound, Ultrason. Sonochem. 18, 226-230.

Mazue, G., Viennet, R., Hihn, J. Y., Carpentier, L., Devidal, P., Albaina, I., 2011. Large-scale ultrasonic cleaning system: Design of a multi-transducer device for boat cleaning (20 kHz), Ultrason. Sonochem. 18, 895-900.

Moncoffre, N., Toulhoat, N., Bérerd, N., Pipon, Y., Silbermann, G., Blondel, A., Galy, N., Sainsot, P., Rouzaud, J. N., Deldicque, D., Dauvois, V., 2016. Impact of radiolysis and radiolytic corrosion on the release of 13C and 37Cl implanted into nuclear graphite: Consequences for the behaviour of 14C and 36Cl in gas cooled graphite moderated reactors, J. Nucl. Mater. 472, 252-258.

Morris, R., Chemical Decontamination for Decommissioning (DFD) and DFDX, 2011.

Moutarlier, V., Viennet, R., Gigandet, M. P., Hihn, J. Y., 2020. Use of ultrasound irradiation during acid etching of the 2024 aluminum alloy: Effect on corrosion resistance after anodization, Ultrason. Sonochem. 64.

Moutarlier, V., Viennet, R., Rolet, J., Gigandet, M. P., Hihn, J. Y., 2015. Power ultrasound irradiation during the alkaline etching process of the 2024 aluminum alloy, Appl. Surf. Sci. 355, 26-31.

Murthy, T. K. S., 1988. Mineral processing in the Indian nuclear energy programme, Bull. Mater. Sci. 10, 403-410.

Muzeau, B., Le Flem, M., Rébiscoul, D., Stefan, L., Darquennes, A., Volovitch, P., DECIMAL - Phenomenological description of the corrosion and its impact on the durability of encapsulated magnesium wastes in hydraulic binders, Nuwcem 2018, Avignon , France.

Nipruk, O. V., Knyazev, A. V., Chernorukov, G. N., Pykhova, Y. P., 2011. Synthesis and study of hydrated uranium(VI) oxides, UO3·nH2O, Radiochemistry 53, 146-150.

Nogita, K., Ockert, S., Pierce, J., Greaves, M. C., Gourlay, C. M., Dahle, A. K., 2009. Engineering the Mg–Mg2Ni eutectic transformation to produce improved hydrogen storage alloys, Int. J. Hydrogen Energy 34, 7686-7691.

O'Hare, P. A. G., Boerio, J., Fredrickson, D. R., Hoekstra, H. R., 1977. Thermochemistry of uranium compounds IX. Standard enthalpy of formation and high-temperature thermodynamic functions of magnesium uranate (MgUO4) A comment on the non-existence of beryllium uranate, The Journal of Chemical Thermodynamics 9, 963-972.

Ogawa, S., Niwa, H., Nakanishi, K., Ohta, T., Yagi, S., 2011. Influence of CO₂ and H₂O on Air Oxidation of Mg Nanoparticles Studied by NEXAFS, Journal of Surface Analysis 17, 319-323.

Pageot, J., Rouzaud, J. N., Ali Ahmad, M., Deldicque, D., Gadiou, R., Dentzer, J., Gosmain, L., 2015. Milled graphite as a pertinent analogue of French UNGG reactor graphite waste for a CO2 gasification-based treatment, Carbon 86, 174-187.

Palacios, M. L., Taylor, S. H., 2000. Characterization of Uranium Oxides Using in Situ Micro-Raman Spectroscopy, Appl. Spectrosc. 54, 1372-1378.

Poncet, F., Valdivieso, F., Gibert, R., Pijolat, M., 1999. In situ infrared spectroscopic study on uranium oxides during UO3 carboreduction, Mater. Chem. Phys. 58, 55-57.

Pushkareva, G. I., Bobyleva, S. A., 2003. Influence of Ultrasound on the Sorption Properties of Brucite, Journal of Mining Science 39, 616-620.

Pushkaryova, G. I., 1999. Sorption extraction of metals from mono-and multicomponent solutions using brucite, Journal of Mining Science 35, 660-663.

Rastoin, J., Brisbois, J., 1978. Gas cooled reactor experience and programs in France, Annals of Nuclear Energy 5, 455-488.

Rooses, A., Lambertin, D., Chartier, D., Frizon, F., 2013. Galvanic corrosion of Mg–Zr fuel cladding and steel immobilized in Portland cement and geopolymer at early ages, J. Nucl. Mater. 435, 137-140.

Serizawa, H., Shiratori, T., Fukuda, K., Fujino, T., Sato, N., 1995. Study on the development of the lattice strain in (Mg,U)O2+x solid solution, J. Alloys Compd. 218, 149-156.

Silva, L. A., Lameiras, F. S., Santos, A. M. M. d., Ferraz, W. B., Barbosa, J. B. S., 2017. Determination of U3O8 in UO2 by infrared spectroscopy, REM - International Engineering Journal 70, 59-62.

Song, G., 2005. Recent Progress in Corrosion and Protection of Magnesium Alloys, Adv. Eng. Mater. 7, 563-586.

Song, G., StJohn, D., 2002. The effect of zirconium grain refinement on the corrosion behaviour of magnesium-rare earth alloy MEZ, Journal of Light Metals 2, 1-16.

Song, G. L., Atrens, A., 2003. Understanding magnesium corrosion - A framework for improved alloy performance, Adv. Eng. Mater. 5, 837-858.

Su-xia, H., Ji-jun, L., Bin, H., Ru-song, L., Tao, S., 2014. The treatment of radioactive wastewater by ultrasonic standing wave method, J. Hazard. Mater. 274, 41-45.

Sun Fangfang, L. N. G., Li Qunying, Liu Enzuo, He Chunnain, Shi Chunsheng, Zhao Naiqin, 2017. Effect of Sc and Zr additions on microstructures and corrosion behavior of Al-Cu-Mg-Sc-Zr alloys, Journal of Materials Science & Technology 33, 1015-1022.

Sweet, L., Reilly, D., Abrecht, D., Buck, E., Meier, D., Su, Y.-F., Brauer, C., Schwantes, J., Tonkyn, R., Szecsody, J., Blake, T., Johnson, T., Spectroscopic studies of the several isomers of UO3, SPIE, 2013.

Tyrpekl, V., Vigier, J. F., Manara, D., Wiss, T., Blanco, O. D., Somers, J., 2015. Low temperature decomposition of U(IV) and Th(IV) oxalates to nanograined oxide powders, J. Nucl. Mater. 460, 200-208.

Van Nguyen, T., Phong Huynh Nguyen, T., Cong Le, H., 2019. The effects of hydrogen peroxide solution and ultrasound on the dissolution of electrodeposited uranium oxide, J Radioanal Nucl Ch 319, 1321-1329.

Verdan, S., Burato, G., Comet, M., Reinert, L., Fuzellier, H., 2003. Structural changes of metallic surfaces induced by ultrasound, Ultrason. Sonochem. 10, 291-295.

Virot, M., Chave, T., Nikitenko, S. I., Shchukin, D. G., Zemb, T., Mohwald, H., 2010. Acoustic Cavitation at the Water-Glass Interface, J. Phys. Chem. C 114, 13083-13091.

Virot, M., Pflieger, R., Ravaux, J., Nikitenko, S. I., 2011. Sonoluminescence of Tb(III) at the Extended Solid-Liquid Interface, J. Phys. Chem. C 115, 10752-10756.

Virot, M., Pflieger, R., Skorb, E. V., Ravaux, J., Zemb, T., Mohwald, H., 2012. Crystalline Silicon under Acoustic Cavitation: From Mechanoluminescence to Amorphization, J. Phys. Chem. C 116, 15493-15499.

Wang, C., Sun, M., Zheng, F., Peng, L., Ding, W., 2014. Improvement in grain refinement efficiency of Mg–Zr master alloy for magnesium alloy by friction stir processing, Journal of Magnesium and Alloys 2, 239-244.

Wang, Y., Chen, Y., Liu, C., Yu, F., 2018. Preparation of porous magnesium oxide foam and study on its enrichment of uranium, J. Nucl. Mater. 504, 166-175.

Wells, H., 1965. Radioactive contamination and its removal by ultrasound, Ultrasonics 3, 211.

Wells, H., 1966. Radioactive decontamination by ultrasonics, Ultrasonics 4, 29-34.

Wen, L. H., Ji, Z. S., Hu, M. L., Ning, H. Y., 2014. Microstructure and mechanical properties of Mg–3.0Nd–0.4Zn–0.4Zr magnesium alloy, Journal of Magnesium and Alloys 2, 85-91.

Wozniak, N., Spectroscopic Signatures of Uranium Speciation for Forensics, in, UNLV Theses, Dissertations, Professional Papers, and Capstones, 2017.

Yan, H., Bai, J., Chen, X., Wang, J., Zhang, H., Liu, Q., Zhang, M., Liu, L., 2013. High U(vi) adsorption capacity by mesoporous Mg(OH)2 deriving from MgO hydrolysis, RSC Adv. 3, 23278-23289.

Yao, Y., Pan, Y., Liu, S., 2020. Power ultrasound and its applications: A state-of-the-art review, Ultrason. Sonochem. 62, 104722.

Zainal Abidin, N. I., Atrens, A. D., Martin, D., Atrens, A., 2011. Corrosion of high purity Mg, Mg2Zn0.2Mn, ZE41 and AZ91 in Hank's solution at 37°C, Corros. Sci. 53, 3542-3556.

Zeng, R.-C., Yin, Z.-Z., Chen, X.-B., Xu, D.-K., Corrosion Types of Magnesium Alloys, in: IntechOpen (Ed.) Magnes. Alloys - Sel. Issue (2018), Tański, T.; Borek, W. and Król, M., 2018, pp. 29-52.

Zeng, R. C., Zhang, J., Huang, W. J., Dietzel, W., Kainer, K. U., Blawert, C., Ke, W., 2006. Review of studies on corrosion of magnesium alloys, Transactions of Nonferrous Metals Society of China 16, S763-S771.

Zhuang, Z., Ou, X., Li, J., Zhou, Y., Zhang, Z., Dong, S., Lin, Z., 2016. Interfacial Engineering Improved the Selective Extraction of Uranyl from Saline Water by Nano-Mg(OH)2 and the Underlying Mechanism, ACS Sustainable Chemistry & Engineering 4, 801-809.

Sonochemical Decontamination of Magnesium and Magnesium-Zirconium Alloys in Mild Conditions

Ran Ji, Matthieu Virot, Rachel Pflieger, Sergey I Nikitenko

ICSM, Univ Montpellier, UMR 5257, CEA, CNRS, ENSCM, Marcoule, France

TOC graphic